

Lesion Harvester: Iteratively Mining Unlabeled Lesions and Hard-Negative Examples at Scale

Jinzheng Cai*, Adam P. Harrison, Youjing Zheng, Ke Yan, Yuankai Huo, Jing Xiao, Lin Yang, Le Lu

Abstract—Acquiring large-scale medical image data, necessary for training machine learning algorithms, is frequently intractable, due to prohibitive expert-driven annotation costs. Recent datasets extracted from hospital archives, *e.g.* DeepLesion, have begun to address this problem. However, these are often incompletely or noisily labeled, *e.g.* DeepLesion leaves over 50% of its lesions unlabeled. Thus, effective methods to harvest missing annotations are critical for continued progress in medical image analysis. This is the goal of our work, where we develop a powerful system to harvest missing lesions from the DeepLesion dataset at high precision. Accepting the need for some degree of expert labor to achieve high fidelity, we exploit a small fully-labeled subset of medical image volumes and use it to intelligently mine annotations from the remainder. To do this, we chain together a highly sensitive lesion proposal generator and a very selective lesion proposal classifier. While our framework is generic, we optimize our performance by proposing a 3D contextual lesion proposal generator and by using a multi-view multi-scale lesion proposal classifier. These produce harvested and hard-negative proposals, which we then re-use to finetune our proposal generator by using a novel hard negative suppression loss, continuing this process until no extra lesions are found. Extensive experimental analysis demonstrates that our method can harvest an additional 9,805 lesions while keeping precision above 90%. As these harvested lesions represent a significant enhancement of an already invaluable dataset, we publicly release them, along with a new test set of *completely* annotated DeepLesion volumes. We also present a pseudo 3D IoU evaluation metric, demonstrating that it corresponds much closer to the real 3D IoU than the current evaluation metric used in DeepLesion. To demonstrate the benefits of our approach, we show that lesion detectors trained on our harvested lesions can significantly outperform the same variants only trained on the original annotations, with boost of average precision of 7 to 10%. We open source our code and annotations at <https://github.com/JimmyCai91/DeepLesionAnnotation>.

Index Terms—Lesion harvesting, lesion detection, hard negative mining, pseudo 3D IoU.

I. INTRODUCTION

PARALLELING developments in computer vision, recent years have seen the emergence of large-scale medical image databases [1]–[5]. These are seminal milestones in

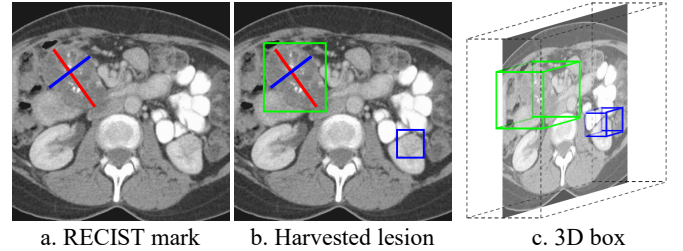


Fig. 1: (a) depicts an example of a RECIST marked CT slice. RECIST marks may be incomplete by both not including co-existing lesions, *e.g.* the blue 2D box in (b), or by not covering the 3D extent of lesions in other slices, *e.g.* the green and blue 3D boxes in (c). We aim to complete lesion annotations in both senses of (b) and (c).

medical imaging analysis research that help address the data-hungry needs of deep learning and other machine learning technologies. Yet, most of these databases are collected retrospectively from hospital picture archiving and communication systems (PACSs), which house the medical image and text reports from daily radiological workflows. While harvesting PACSs will likely be essential toward truly obtaining large-scale medical imaging data [6], their data are entirely ill-suited for training machine learning systems [7] as they are not curated from a machine learning perspective. As a result, popular large-scale medical imaging datasets suffer from uncertainties, mislabellings [3], [8], [9] and incomplete annotations [5], a trend that promises to increase as more and more PACS data is exploited. Correspondingly, there is a great need for effective data curation, but, unlike in computer vision, these problems cannot be addressed by crowd-sourcing approaches [10], [11]. Instead this need calls for alternative methods tailored to the demanding medical image domain. This is the focus of our work, where we articulate a powerful and effective label completion framework for lesion datasets, applying it to harvest unlabeled lesions from the recent DeepLesion dataset [5].

DeepLesion [4], [5] is a recent publicly released medical image database of CT sub-volumes along with localizations of lesions. These were mined from computed tomography (CT) scans from the US National Institutes of Health Clinical Center PACS. The mined lesions were extracted from response evaluation criteria in solid tumours (RECIST) [12] marks performed by clinicians to measure tumors in their daily workflow. See Fig. 1(a) for an example of a RECIST marked lesion. In total, DeepLesion contains 32,735 retrospectively clinically annotated lesions from 10,594 CT scans of 4,427

J. Cai, A. P. Harrison, K. Yan, Y. Huo, and L. Lu are with PAII Inc., Bethesda, MD 20817, USA. (email: caijinzhengcn@gmail.com, adampharrison070@pail-labs.com, yanke383@pail-labs.com, huoyuankai@gmail.com, le.lu@pail-labs.com). Y. Huo is now with Vanderbilt University.

J. Xiao is with Ping An Insurance (Group) Company of China, Ltd., Shenzhen, 510852, PRC. (email: xiaojing661@pingan.com.cn)

Y. Zheng is with Virginia Polytechnic Institute and State University, Blacksburg, VA 24061, USA. (email: zhengyoujing@vt.edu)

L. Yang is with University of Florida, Gainesville, FL 32611, USA. (email: linyang711@gmail.com)

Corresponding author: Jinzheng Cai

unique patients. A variety of lesion types and subtypes have been included in this database, such as lung nodules, liver tumors, and enlarged lymph nodes. As such, the DeepLesion dataset is an extremely important source of data for medical imaging analysis tasks, including training and characterizing lesion detectors and for developing radiomics-based biomarkers for tumor assessment and tracking. However, due to the RECIST guidelines [12] and workload limits, physicians typically marked only a small amount of lesions per CT scan as the *finding(s) of interest*. Yet, as shown in Fig. 1(b), more often than not CT images exhibit multiple co-existing lesions per patient. Indeed, based on a recent empirical study [13], and our own results presented later, there are about the same quantity of missing findings compared to reported ones. Moreover, as Fig. 1(c) illustrates, RECIST marks do not indicate the 3D extent, leaving tumor regions of the same instance in adjoining slices unmarked. This severely challenges the development of high-fidelity disease detection algorithms and artificially limits the dataset’s usefulness for biomarker development. Nevertheless, it is highly impractical and infeasible to recruit physicians to manually revise and add back annotations for the entire database.

To address this issue, we aim to reliably discover and harvest unlabeled lesions. Given the expert-driven nature of annotations, our approach accepts the need for a small amount of supplementary physician labor. It integrates three processes: (1) a highly sensitive detection-based lesion proposal generator (LPG) to generate lesion candidates, (2) manual verification of a small amount of the lesion proposals, and (3) a very selective lesion proposal classifier (LPC) that uses the verified proposals to automatically harvest prospective positives and hard negatives from the rest. These processes are tied together in an iterative fashion to strengthen the lesion harvesting at each round. Importantly, for (1) and (3) our framework can accept any state-of-the-art detector and classifier, allowing it to benefit from future improvements in these two domains. However, in this work, we develop our own LPG, called multi-slice CenterNet (MSCN), that combines the recent innovations seen in CenterNet [14] and the multitask universal lesion analysis network (MULAN) [15]. We also propose a hard negative suppression loss (HNSL) to boost our LPG with harvested hard negative cases. Among choices of LPCs, we use a multi-view convolutional neural network (CNN) to further reduce the false positive rate of produced lesion proposals. With our framework, we are able to harvest an additional 9,805 lesions from DeepLesion, while keeping the label precision above 90%, at a cost of only fully annotating 5% of the data. Compared to the original dataset this is a boost of 24.9% in recall rates. Thus, our lesion harvesting framework, along with the introduced MSCN LPG and HNSL, represent our main contributions.

However, we also provide additional important contributions. For one, we completely annotate and publicly release 1915 of the DeepLesion subvolumes with RECIST marks, in addition to our harvested lesions. Second, we introduce and validate a new pseudo 3D (P3D) evaluation metric, designed for completely annotated data, that serves as a much better measurement of 3D detection performance than

current practices. Since all DeepLesion test data, up to this point, is incompletely annotated, these contributions provide an invaluable resource and method for more accurately evaluating lesion detection systems. Finally, we report concrete benefits of harvesting unlabeled lesions. To do this, we train several state-of-the-art detection systems [14], [16] using data augmented with our harvested prospective lesions and hard negative examples. We show that with even the best published method to date [15], average precision (AP) can be improved by 10 percent. We also show that our MSCN LPG can also be used as an extremely effective detector, outperforming the state-of-the-art and providing additional methodological contributions to the lesion detection topic.

II. RELATED WORK

Detection with incomplete ground-truth. To reduce the effect of missing labels, Ren *et al.* [17] only used true positives and hard negatives for training detectors, where the latter were defined as region proposals with at least an overlap of 0.1 with existing ground truth boxes. This setup, which we denote overlap-based hard sampling (OBHS), should help mitigate false negatives; however, it inevitably sacrifices a large amount of informative true negatives that have ≤ 0.1 overlap with ground truth boxes. Wu *et al.* [18] proposed overlap-based soft sampling (OBSS) to improve object detectors, which weights contributions of region proposals proportional to their overlap with the ground truth. These strategies reduce the impact of true negatives not overlapping with the ground truth. Yet, true negatives in the background body structures are usually informative for training a robust lesion detector. By explicitly attempting to harvest prospective positives, our approach minimizes false negatives without suppressing informative background regions.

Label propagation from partial labels. Our work also relates to efforts on knowledge distillation and self label propagation. Radosavovic *et al.* [19] proposed a data distillation method to ensemble predictions and automatically generate new annotations for unlabeled data from internet-scale data sources. Gao *et al.* [20] investigated propagating labels from fully-supervised interstitial lung disease masks to unlabeled slices using CNNs and conditional random fields. Cai *et al.* [21] recovered 3D segmentation masks from 2D RECIST marks in DeepLesion by integrating a CNN and GrabCut [22] to incrementally propagate segmentation masks from the central RECIST-marked slice to consecutive upper and lower slices. We also tackle the large-scale and noisy DeepLesion dataset, but we process each CT volume as a whole, rather than focus on post-processing a given region of interest.

Lesion detection. Yan *et al.* [4] introduced the DeepLesion dataset, which is an invaluable large-scale clinical database for whole body lesion detection, with followup work focusing on incorporating 3D context into 2D two-stage region-proposal CNNs [13], [15]. These work demonstrate the importance of incorporating 3D context in lesion detection and currently represent the state-of-the-art performance on DeepLesion. Some recent works also investigated one-stage detectors [23], [24].

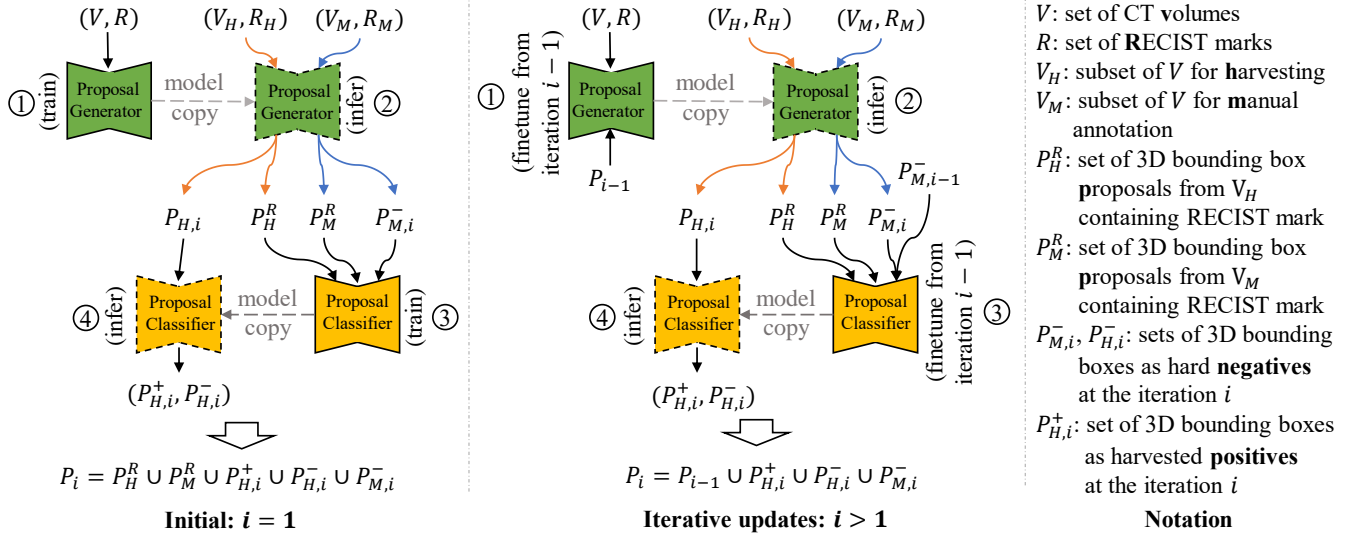


Fig. 2: The framework of our proposed iterative lesion completion approach. The first and second columns depict the initial iteration and follow-up iterations, respectively, where we use ①, ②, ③, and ④ to indicate the sequence of operations. In step ①, we train (or finetune) the LPG, and then, in step ②, we apply it on V_H and V_M to generate 3D proposals. In step ③, we train/finetune the LPC, and apply it in step ④ to automatically separate proposals into positive and negative groups as $P_{H,i}^+$ and $P_{H,i}^-$, respectively.

Compared with two-stage detectors, one-stage detectors are more flexible, straightforward, and computationally efficient. For instance, two-stage detectors can require significant hyperparameter tuning in their anchor configuration to meet performance expectations [24]. Finally, there are recent work focusing on relevant task specific settings. For instance, Dou *et al.* [25] and Ding *et al.* [26] suggested using 3D CNNs to further reduce false positive rates and Tang *et al.* [27] showed that hard negative mining can increase detection sensitivity by considerable margins.

Unlike the above work, our main focus is on label harvesting on *seen* datasets. To do so, we demonstrate how to incorporate the state-of-the-art detection frameworks as an LPG for label completion. We also introduce a one-stage multi-slice LPG that performs better than prior work. Like Tang *et al.* [27], we also demonstrate the importance of hard negative mining. Finally, with our lesion harvesting task completed, we then show how the complete labels can be used to train the same LPG detection frameworks for better localizing lesions on *unseen* datasets.

III. METHODS

Fig. 2 overviews our proposed iterative lesion harvesting approach. As motivated above, we aim to harvest missing annotations from the incomplete DeepLesion dataset [4], [5]. Additionally, as Fig. 1(c) demonstrates, another important facet of our completion strategy is to fully localize the 3D extent of lesions, which means we aim to also generate 3D proposals for both RECIST-marked and missing lesions. We first overview our method in Sec. III-A and then detail each component in Sec.s III-B–III-E. This is followed by Sec. III-F, which outlines our proposed pseudo 3D (P3D) evaluation metric.

A. Overview

For the problem setup, we assume we are given a set of N incompletely labeled CT volumes, V , along with 2D RECIST marks for each volume, R . Each volume is associated with a set of lesions, some of which may be RECIST-annotated and some of which may be unannotated. Our goal is to discover the unlabeled lesions and harvest a set of 3D lesion bounding boxes that cover both the RECIST-marked and unannotated lesions. To do this, we assume we have a *completely* annotated subset of N_M volumes¹, V_M . This can be accomplished by supplementing the original DeepLesion RECIST marks for V_M . The remainder of volumes we wish to harvest from are denoted V_H , and we wish to exploit V_M to harvest lesions from V_H . Importantly, $N_M \ll N$ to keep labor requirements low.

In the initial iteration, we start by training a lesion proposal generator (LPG) using the original and supplemental RECIST marks. To keep our framework flexible, any state-of-the-art lesion detection system can be used, either an off-the-shelf variant or the customized MSCN approach we elaborate in Sec. III-B. After convergence, we then execute the trained LPG on V , producing a set of 3D lesion proposals, P_G . These likely cover a large number of lesions, but they may suffer from high false positive rates. To correct this, we divide P_G into P_M and P_H , which are proposals generated from V_M and V_H , respectively. Because V_M are completely RECIST-annotated, we can divide P_M into true positive and false positive proposals, denoted P_M^R and P_M^- , respectively. We also collect proposals from V_H that cover the original RECIST marks, P_H^R , which can be used as another source of positives. We then use P_M^R , P_M^- , and P_H^R to train a binary lesion

¹In DeepLesion, these are actually sub-volumes of whole-body CT scans.

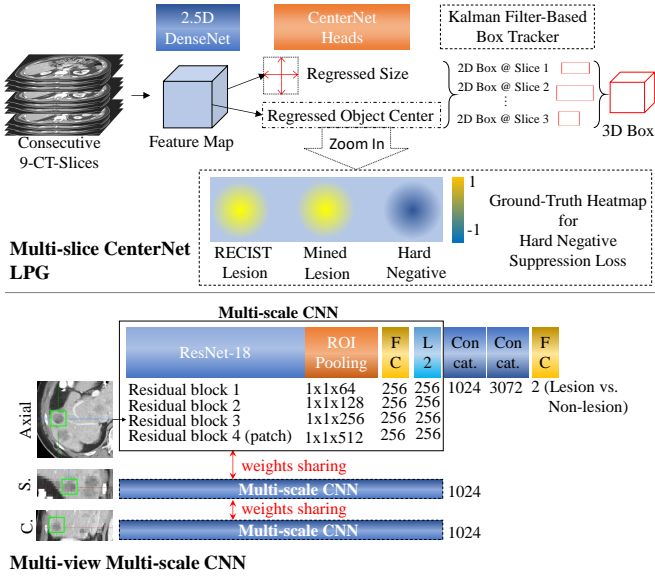


Fig. 3: (Up): Our proposed MSCN LPG combines the CenterNet [14] framework with MULAN-style 2.5D contextual fusion [15]. A Kalman filter-based method is used to create 3D bounding boxes from 2D lesion proposals. We also show example ground truth heatmaps for the proposed HNSL loss, which incorporates hard negative examples. (Down): Our LPC separately processes lesion proposals in axial, sagittal (S.), and coronal (C.) views, fusing their features before a final fully-connected layer.

proposal classifier (LPC). Like the LPG, any generic solution can be used; however, we show that a multi-view classification approach is particularly useful. The trained LPC is then used to classify P_H into P_H^+ , P_H^- , which are the designated positive and negative proposals, respectively.

In the following iterations, the result of the previous iteration is a set of new harvested positive and negative 3D proposals, $P_1 = P_{H,1}^+ \cup P_{H,1}^- \cup P_{M,1}^R \cup P_{M,1}^-$. To refine the process further, we can use P to finetune the LPG and begin the process anew. Importantly, when retraining the LPG, we use $P_{H,1}^+$ and $P_{M,1}^-$ as mined hard negatives. Each round, i , provides a set of harvested proposals, $P_{H,i}^+$ and updates the pool of lesion proposals $P_i = P_{i-1} \cup P_{H,i}^+ \cup P_{H,i}^- \cup P_{M,i}^-$. In addition, P_M^R and P_H^R provide 3D bounding boxes for lesions that were previously only annotated with 2D RECIST marks. Thus, this process generates a more complete and richly annotated dataset. For clarity, we drop the i , unless needed, for the remainder of this work. Below, we elaborate further on the individual system components.

B. Lesion Proposal Generation

1) *Multi-Slice CenterNet (MSCN)*: The task of our lesion proposal generator (LPG) is to produce as high-quality lesion candidates as possible. While any state-of-the-art detection system can serve as LPG, there are attributes which are beneficial. An LPG with high sensitivity will help recover unlabeled lesions. Meanwhile, if it retains reasonable specificity, it will make downstream classification of proposals into true- and

false-positives much more feasible. Computational efficiency is also important, to not only make training scalable, but also to be efficient in processing large amounts of CT images. Finally, simplicity and efficiency are also crucial virtues, as the LPG will be one component in a larger system.

To avoid prohibitive computational and memory demands, we opt for using a 2D-based detection approach, which is the defacto standard in lesion detection [13], [15], [23], [24], [24], [27], [28]. Our LPG of choice is a multi-slice CenterNet (MSCN), which combines state-of-the-art one-stage anchor-free 2D proposal generation [14] with 3D context fusion [15]. Others have articulated the benefits of dense pixel-wise supervision [16], [27] and one-stage approaches provide a more straightforward means to aggregate such signals. Additionally, the choice of an anchor-free approach avoids the need to tune anchor-related hyper-parameters to make the generator robust to various lesion sizes and shapes. Because lesions have convex shapes which have centroids located inside lesions, the center-based loss of CenterNet [14] is a natural choice. A final advantage to the one-stage anchor-free approach, which we will show in Sec. III-E, is that it allows for a natural incorporation of hard negative examples, which significantly improves the lesion detection performance.

We follow the same pipeline and hyper-parameter settings described by Zhou *et al.* [14]. Namely, we create ground-truth heatmaps centered at each lesion using Gaussian kernels $Y \in [0, 1]^{W \times H}$. The training objective is to then produce a heatmap, \hat{Y}_{xy} , using a penalty-reduced pixel-wise logistic regression with focal loss [29]:

$$L_k = \frac{-1}{m} \sum_{xy} \begin{cases} (1 - \hat{Y}_{xy})^\alpha \log(\hat{Y}_{xy}) & \text{if } Y_{xy} = 1 \\ (1 - Y_{xy})^\beta (\hat{Y}_{xy})^\alpha & \text{otherwise} \\ \log(1 - \hat{Y}_{xy}) & \end{cases}, \quad (1)$$

where m is the number of objects in the slice and $\alpha = 2$ and $\beta = 4$ are hyper-parameters of the center loss. At every output pixel, the width, height, and offset of lesions are also regressed, but they are only supervised where $Y_{xy} = 1$. The lesion proposals are produced by combining center points with regressed width and height. See Zhou *et al.* for more details.

To incorporate 3D context, which Yan *et al.* [15] demonstrated can benefit lesion detection, we use a 2.5D DenseNet-121 backbone [30]. This backbone is associated with the highest performance for DeepLesion detection to-date [15]. 3D context is included by inputting 9 consecutive CT slices, including the target slice and the adjoining 4 slices above and below. Fig. 3 depicts the resulting MSCN LPG.

2) *3D Proposal Generation*: Regardless of the LPG used, if it operates slice-wise, like the MSCN, then post-processing is required to generate 3D proposals. To do this, we first apply the LPG to every axial slice. This produces a set of 2D proposals, each with an “objectness” or detection score. Next, we stack proposals in consecutive slices using the same Kalman filter-based bounding box tracker as Yang *et al.* [31]. More specifically, we first select 2D proposals whose detection score is greater than a threshold t_G . 2D proposals from adjoining slices are then stacked together if their intersection over union (IoU) is greater than 0.8. Finally, in case the LPG

misses lesions in intermediate slices, we extend each 3D box up and down by one slice, and if any two 3D boxes become connected with ≥ 0.8 overlap on the connecting slices, then they will be fused as one 3D proposal. When lesion harvesting, we choose 0.1 as the value for t_G which helps keep the number of proposals manageable. However, our experience indicates that results are not sensitive to significant deviations from our chosen threshold value.

C. Manual Verification

The next step in our process is to separate lesion candidates into true- and false-positives. As mentioned above, we assume a labor budget to fully annotate a small subset of volumes, V_M , with RECIST marks. Within V_M , we can identify the 3D proposals that overlap (see Sec. III-F) with the RECIST marks to be true-positives and denote them as P_M^R . The remaining false-positive proposals are denoted P_M^- . In addition to the fully annotated V_M , we can also identify true-positives P_H^R , which are the proposals that overlap with the RECIST marks in V_H . Because V_H is only partially labeled, the remainder of proposals in the subset can be either true- or false-positives. These three sets of classified proposals, P_M^R , P_M^- , and P_H^R , can now serve as training instances to further filter the remaining proposals from V_H .

D. Mining Prospective Positives and Hard Negatives

With the manually verified proposals in hand, namely P_M^R , P_M^- , and P_H^R , the aim is to identify the remaining proposals in the harvesting subset V_H . To do this, we use the verified proposals to train a lesion proposal classifier (LPC). In principle, any classifier can be used, but we apply a multi-view CNN classifier that incorporates 3D context by separately processing axial, coronal, and sagittal slices generated from each proposal center point to produce 3 global features. The resulting features are then concatenated together before being processed by a fully-connected layer. This is based on the intuition that 3D context is necessary for differentiating true positive lesion proposals from false positives [25], [26], whether for machines or for clinicians. Such multi-view setups have been shown to boost performance for lesion characterization [32] and have the virtue of offering a much more computational and memory efficient means to encode 3D context compared to true 3D networks.

We choose to use a ResNet-18 [33] as our backbone because of its proven usefulness and availability of pre-trained weights. The LPC is trained with the RECIST verified proposals, P_M^R , P_M^- , and P_H^R . We expect this combination to be representative to the actual distribution of lesions in DeepLesion. In particular, although the negative samples are only generated from V_M , they should also be representative to the dataset-wide distribution of hard negatives since the hard negatives are typically healthy body structures, which are common across patients. Fig. 3 depicts our chosen LPC.

With the LPC trained, we then apply it to the proposals needing harvesting: P_H/P_H^R . Since the LPG and LPC are independently trained, we make an assumption, for simplicity,

that their pseudo-probability outputs are independent as well. Thus, the final score of a 3D proposal can be calculated as

$$s_{g,c} = s_g s_c, \quad (2)$$

where $s_{g,c}$ is called the lesion score and s_g and s_c are the LPG objectness score and LPC classification probability, respectively. We obtain the former by taking the max detection score across all 2D boxes in the proposal. Based on $s_{g,c}$, we generate prospective positive proposals, P_H^+ , by choosing a threshold for $s_{g,c}$ that corresponds to a precision above 95% on the completely annotated set V_M . We select hard-negatives from proposals not meeting this criterion. More specifically, from this remainder we first select any whose detection scores, s_g , were ≥ 0.5 . Then, from each subvolume we choose up to five proposals with the top detection scores. This selects for proposals with high objectness scores that were later filtered by the LPC.

E. Iterative Updating

After a round of harvesting, we repeat the process by finetuning the LPG, but with two important differences. First, because we have 3D proposals, we have access to additional 2D slices, and accompanying bounding boxes, to feed into training. Second, we incorporate mined lesions and hard negatives to further improve our proposal generation. To keep computational demands reasonable, only the 2D slices with the highest objectness score within each proposal of $P_M^R \cup P_M^- \cup P_H^R \cup P_H^+ \cup P_H^-$ are used.

To incorporate harvested hard negative proposals, we use the same procedure in Sec. III-B, but replace the center-loss in Eq. 1 with our proposed hard negative suppression loss (HNSL). To do this, we create separate heat maps for positive (RECIST-marked or prospective positive) and hard-negative lesions. We denote these heat maps as Y_{xy}^p and Y_{xy}^n , respectively. We then create a master ground truth heat map, Y_{xy} , by overwriting Y_{xy}^p with Y_{xy}^n :

$$Y_{xy} = \begin{cases} -Y_{xy}^n & \text{if } Y_{xy}^n > 0 \\ Y_{xy}^p & \text{otherwise} \end{cases}. \quad (3)$$

The result is a ground truth map that can now range from $[-1, 1]$. When used in the loss of (1), the effect is that positive predictions in hard negative regions are penalized much heavier than standard negative regions (16 times heavier when $\beta = 4$). This simple modification works surprisingly well for further reducing false positive rates. We visually depict example ground truth heatmaps in Fig. 3.

F. Pseudo-3D Evaluation

Apart from the lesion completion framework, introduced above, another important aspect to discuss is evaluation. Current DeepLesion works [13], [15], [23], [24], [24], [27], [28] operate and evaluate only based on the 2D RECIST marks on selected 2D slices that happen to contain said marks. This is problematic, as RECIST-based evaluation will not reflect actual performance: it will miscount *true positives* on unmarked lesions or on adjoining slices as *false positives*. Moreover,

automated methods should process the whole image volume, meaning precision should be correlated to false positives per *volume* rather than per selected *slice*. In this way, automated methods can be more effective on holistically describing and recording tumor existence, complimentary to human efforts to better achieve precision medicine.

Because we aim to harvest 3D bounding boxes that cover all lesions, we must evaluate, by definition, on completely annotated test data. Yet, it is not realistic to assume data will be fully annotated with 3D bounding boxes. Instead, a more realistic prospect is that test data will be completely annotated with 2D RECIST marks, especially by clinicians who are more accustomed to this. Thus, assuming this is the test data available, we propose a pseudo 3D (P3D) IoU metric. For each RECIST mark, we can generate 2D bounding boxes based off of their extent, as in [28]. This we denote $(x_1, x_2, y_1, y_2, z, z)$, where z is the slice containing the mark. Given a 3D bounding box proposal, $(x'_1, x'_2, y'_1, y'_2, z'_1, z'_2)$, our P3D IoU metric will be counted as a true positive if and only if $z'_1 \leq z \leq z'_2$ and $\text{IoU}[(x_1, x_2, y_1, y_2), (x'_1, x'_2, y'_1, y'_2)] \geq 0.5$. Otherwise, it is considered a false positive. Because we publicly release complete RECIST marks of 1915 volumes, the P3D IoU metric can also be used to benchmark DeepLesion detection performance, replacing the one currently used. As we show in the results, the P3D IoU metric is a much more accurate performance measure.

IV. EXPERIMENTS

A. Dataset

To harvest lesions from the DeepLesion dataset, we randomly select 844 volumes from the original 14075 training CTs². These are then annotated by a board-certified radiologist. Of these, we select 744 as V_M (5.3%) and leave another 100 as an evaluation set for lesion harvesting. This latter subset, denoted V_H^{test} , is treated identically at V_H , meaning the algorithm only sees the original DeepLesion RECIST marks. After convergence, we can measure the precision and recall of the harvested lesions. In addition, we later measure detection performance on systems trained on our harvested lesions by also fully annotating 1,071 of the testing CT volumes. These volumes, denoted V_D^{test} , are never seen in our harvesting framework.

B. P3D IoU Evaluation Metric

Before validating our lesion harvesting framework, we first validate our proposed P3D metric. To do this, we fully annotated a small set of 272 CT test volumes, randomly selected from V_D^{test} , with 3D bounding boxes. From these, we can calculate a “gold-standard” 3D IoU metric, and analyze how well the current incomplete 2D RECIST metric and our P3D metric can act as a proxy. Accordingly, we trained state-of-the-art detection methods (the same 12 outlined in Table III’s later experiments) on the DeepLesion dataset and measured their performance using 3D IoU, incomplete RECIST [28], and the proposed P3D IoU metrics. Here use a 3D IoU

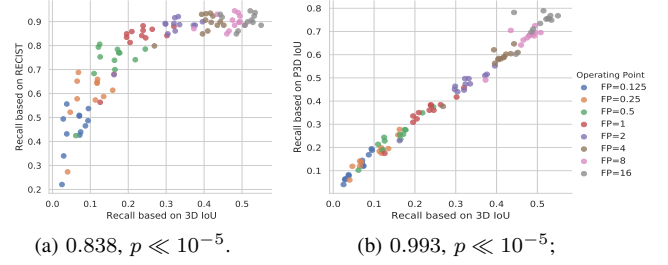


Fig. 4: Comparing the concordance of the incomplete 2D RECIST and our P3D metric compared to the gold-standard 3D IoU metric. For each metric, lesion detection recalls at operation points from FP=0.125 to FP=16 are collected from the FROC curves of 12 lesion detection methods. Pearson coefficients are shown below each chart.

TABLE I: Lesion harvesting performance evaluated on V_H^{test} . Detection recalls (R) at precisions (P) from 80% to 95% are reported after three harvesting rounds.

Training Label Set	R@80P	R@85P	R@90P	R@95P
R	0.364@100P			
$R \cup P_{H,1}$	0.560	0.509	0.489	0.476
$R \cup P_{H,1}^+$	0.591	0.572	0.545	0.497
$R \cup P_{H,1}^+ \cup P_{H,2}^+$	0.678	0.651	0.585	0.512
$R \cup P_{H,1}^+ \cup P_{H,2}^+ \cup P_{H,3}^+$	0.668	0.649	0.613	0.498

threshold of 0.33, instead of 0.5 used for the 2D metrics, to help compensate for the severity of 3D IoU. As shown in Fig. 4b and Fig. 4a, we measured FROC curves and compare detection recalls of these methods at operating points varying from false positive (FP) rates of 0.125 to 16 per volume. As can be seen, our P3D metric has much higher concordance with the true 3D IoU than does the incomplete 2D RECIST metric. Moreover, the latter exhibits a relationship that is much noisier and non-monotonic, making it likely any ranking of methods does not correspond to their true ranking. Thus, for the remainder of this work we report lesion harvesting and lesion detection performance using only the P3D metric. Moreover, we advocate using the P3D metric, and the fully RECIST-annotated test sets we publicly release, to evaluate DeepLesion detection systems going forward.

C. Main Result: Lesion Harvesting

We validate our lesion harvesting by running it for 3 rounds. As can be seen in Table I, the original RECIST marks only have a recall of 36.4% of existing lesions in the V_H^{test} set, with an assumed precision of 100%. However, after one iteration, the initial lesion proposals generated by the MSCN LPG, denoted as $P_{H,1}$, can already boost the recall to 48.9%, while keeping the precision at 90%. However, after filtering with our LPC, i.e. the $R \cup P_{H,1}^+$ proposals, this recall is boosted to 54.5%, representing a roughly 20% increase in recall over the original RECIST marks. This demonstrates the power and usefulness of our LPG and LPC duo. After 3 rounds of

²<https://nihcc.app.box.com/v/DeepLesion>

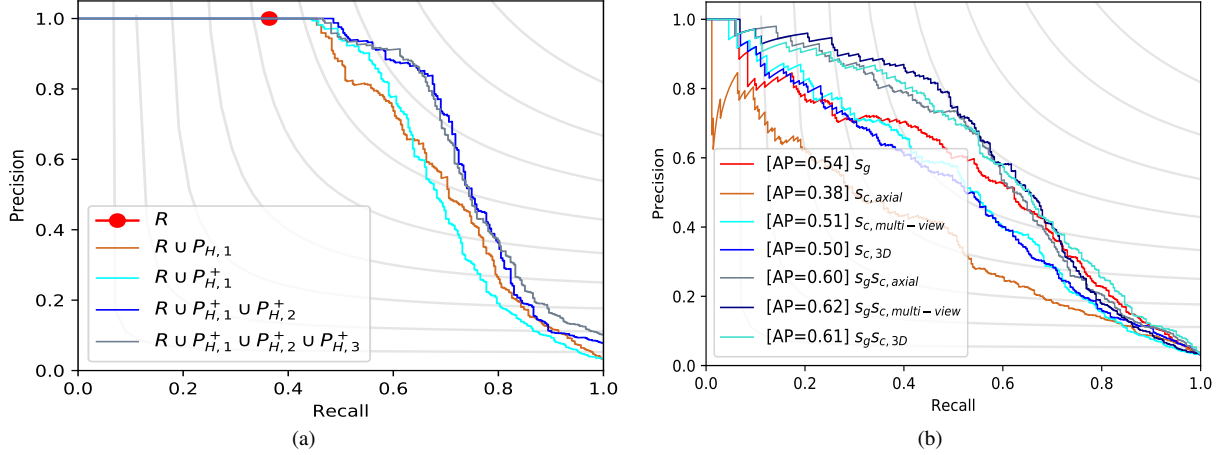


Fig. 5: (a) PR curve evaluating our iterative lesion harvesting procedure. The original RECIST marks only have a recall of 36.4%, which is shown as the red dot. $P_{H,1}$ is the set of lesion proposals from LPG, which are then filtered by the LPC to generate $P_{H,1}^+$. $P_{H,2}^+$ and $P_{H,3}^+$ are harvested lesions from the second and third iterations, respectively. (b) PR curves of LPC variants in the first iteration, where $s_{c,axial}$, $s_{c,multi-view}$, and $s_{c,3D}$ denote classification scores from (2) for 2D axial, 2D multi-view, and 3D LPCs, respectively.

our system, the performance increases further, topping out at 61.3% recall at 90% precision. *This corresponds to harvesting 9,805 more lesions from the V_H CT volumes.* Importantly all 2D lesion bounding boxes are now also converted to 3D. It should be stressed that these results are obtained by annotating 744 volumes, which represents only 5.3% of the original data. In Fig. 5a, we visually depict PR curves. We terminate our lesion harvesting system after 3 rounds where improvements in PR have begun to top out. In our implementation, training LPG and LPC involves 3 NVIDIA RTX6000 GPUs and it takes a few hours to converge. Lesion proposal generation is time consuming since it requires LPG to scan every CT slice in DeepLesion. When paralleled with 4 GPUs and 12 Intel Xeon CPUs, it takes about 12 hours to scan the whole dataset. In total, the proposed pipeline takes 3 days to converge on DeepLesion.

Fig. 6 provides some visual examples of the harvested lesions. As can be seen, lesions missing from the original RECIST marks can be harvested. These examples, coupled with the quantitative boosts in recall (seen in Fig. 5a), demonstrate the utility and power of our lesion harvesting approach.

D. LPG Ablation Study

Table II presents the performance of the MSCN LPG when trained with different combinations of harvested lesions. Please note, that these results only measure the LPG performance, and do not include the effect of the LPC filtering. First, as expected, when including the additional fully labeled proposals, P_M^R , the performance does not improve much over simply using the original RECIST marks. This reflects the relatively small size of V_M compared to the entire dataset. However, larger impacts can be seen when including the hard negatives, $P_{M,i}^-$, from the fully-labeled subset. When including hard negatives from our volumes needing harvesting, i.e. $P_{H,i}^-$, performance boosts are even greater at the high

precision operation points where FPs ≤ 1 . This validates our HNSL approach of using hard-negative cases. Meanwhile, the addition of extra positive samples, $P_{H,i}^+$ and P_H^R , contribute much to the recall when FPs ≥ 2 per volume, as the trained LPG becomes much more sensitive. In sum, these results indicate that the harvested lesions and hard negatives can significantly boost how many lesions can be recovered from the DeepLesion dataset.

E. LPC Ablation Study

We also validate our choice of multi-view LPC. To do this, we compare the performance of different LPCs evaluated on V_H^{test} at the first iteration of our method. We compare our multi-view CNN with two alternatives: a 2D variant that only accepts the axial view as input and a 3D version of ResNet-18 [34] which takes a 3D sub-volume as input. Either 2D patches or 3D sub-volumes are cropped from the original CT volume centered at lesion proposals and padded with 64 pixels in each direction. Results when using the raw “objectness” LPG score, s_g , LPC classification probability, s_c , or the final lesion score, $s_{g,c}$, of Eq. 2, are measured. As can be seen in Fig. 5b, not all LPCs outperform the raw objectness scores. However, they all benefit from the re-scoring of Eq. 2 using the objectness score. Out of all options, the multi-view approach works the best. In addition to its high performance, it also has the virtue of being much simpler and faster than a full 3D approach.

F. Main Result: Detectors Trained on Harvested Lesions

While the above demonstrated we can successfully harvest missing lesions with high precision, it remains to be demonstrated how beneficial this is. To this end, we train state-of-the-art detection systems with and without our harvested lesions and also compare against some alternative approaches to manage missing labels.

TABLE II: Evaluations of LPG trained with different label sets including the original RECIST marks, recovered 3D RECIST-marked lesions P_H^R and P_M^R , mined lesions $\bigcup_{k=1}^{i-1} P_{H,k}^+$, and mined hard negatives $\bigcup_{k=1}^{i-1} P_{H,k}^-$ and $\bigcup_{k=1}^{i-1} P_{M,k}^-$. The recall numbers are extracted from FROC curves at operation points from FP= 0.125 to FP= 8 per volume. Higher recall demonstrates better detection performance.

Exp.	iter. i	R	P_M^R	$\bigcup_{k=1}^{i-1} P_{M,k}^-$	P_H^R	$\bigcup_{k=1}^{i-1} P_{H,k}^+$	$\bigcup_{k=1}^{i-1} P_{H,k}^-$	Recall (%) @ FPs=[0.125,0.25,0.5,1,2,4,8] per volume							
(a)	1	✓						0.120	0.210	0.317	0.457	0.531	0.610	0.669	
(b)	1	✓	✓					0.160	0.217	0.329	0.443	0.557	0.626	0.695	
(c)	2	✓	✓	✓				0.195	0.274	0.369	0.488	0.555	0.648	0.705	
(d)	2	✓	✓	✓	✓			0.179	0.312	0.455	0.524	0.605	0.662	0.726	
(e)	2	✓	✓	✓	✓	✓		0.289	0.355	0.455	0.531	0.576	0.652	0.707	
(f)	2	✓	✓	✓	✓	✓		0.304	0.386	0.471	0.536	0.586	0.626	0.683	
(g)	3	✓	✓	✓	✓	✓	✓	0.255	0.388	0.471	0.543	0.595	0.641	0.717	

TABLE III: Evaluation of detectors trained with and without mined lesions on V_D^{test} .

Method	Backbone	Input	R	P_H^+	P^-	Recall (%) @ FPs=[0.125,0.25,0.5,1,2,4,8] per volume								AP
MULAN [15]	2.5D DenseNet-121	9	✓			11.43	18.69	26.98	38.99	50.15	60.38	69.71	41.8	
Faster R-CNN [17]	2.5D DenseNet-121	9	✓			07.20	13.21	20.97	31.27	43.87	54.92	64.20	34.2	
w/ OBHS [17]	2.5D DenseNet-121	9	✓			02.51	04.77	08.40	17.46	22.65	34.24	47.01	17.3	
w/ OBSS [18]	2.5D DenseNet-121	9	✓			06.85	12.58	21.92	32.39	44.53	57.08	67.91	36.3	
w/ M-OBHS	2.5D DenseNet-121	9	✓			08.53	13.67	22.89	34.46	46.85	58.31	68.08	38.3	
Faster R-CNN	2.5D DenseNet-121	9	✓	✓		10.35	15.98	25.02	35.63	47.15	57.74	66.77	38.5	
CenterNet	DenseNet-121	3	✓			12.91	19.89	26.19	35.77	45.32	56.94	67.83	41.0	
CenterNet	DenseNet-121	3	✓	✓		14.38	19.75	28.04	36.89	46.82	58.94	68.70	42.8	
CenterNet w/ HNSL	DenseNet-121	3	✓	✓	✓	19.26	25.87	34.54	43.17	53.34	63.08	71.68	48.3	
MSCN	2.5D DenseNet-121	9	✓			11.92	18.42	27.54	38.91	50.15	60.76	69.82	43.0	
MSCN	2.5D DenseNet-121	9	✓	✓		13.40	19.16	27.34	37.54	49.33	60.52	70.18	43.6	
MSCN w/ HNSL	2.5D DenseNet-121	9	✓	✓	✓	19.86	27.11	36.21	46.82	56.89	66.82	74.73	51.9	

1) Using Harvested Lesions and Hard Negative Examples:

After our method converged, we fused mined lesions and hard negatives, i.e. $P_H^+ = \bigcup_{i=1}^3 P_{H,i}^+$ and $P_H^- = \bigcup_{i=1}^3 P_{H,i}^-$ and $P_M^- = \bigcup_{i=1}^3 P_{M,i}^-$, respectively. We tested CenterNet [14], Faster R-CNN [16], and our MSCN (used now as a detector instead of an LPG), trained both on the original DeepLesion RECIST marks and on the data augmented with our harvested lesions. Since MULAN requires tags, which are not available for harvested lesions, we only test it using the publicly-released model. As well, we only test the impact of our hard negatives, $P^- = P_H^- \cup P_M^-$, with our proposed HNSL on CenterNet and MSCN. We do not test the HNSL with Faster R-CNN, since it is not compatible with two-stage anchor-based systems. We test all detector variants on the unseen fully labeled V_D^{test} data.

As Table III demonstrates, using the harvested lesions to train detectors can provide significant boosts in recall and precision for all methods. For instance, the extra mined lesions P_H^+ boosts Faster R-CNN's detection performance by 4.3% in average precision. When incorporating hard negatives using the HNSL, CenterNet and MSCN both benefited even more, with additional boosts of 5 – 8% AP. In total, the harvested prospective positive and hard negative lesions are responsible for a boost of 7.2% and 8.9% in AP, for CenterNet and MSCN, respectively, representing a dramatic boost in performance. Finally, we also note that our MSCN outperforms the state-of-the-art lesion detection model, MULAN [15], even when no mined lesions are used. The addition of mined lesions, which is not possible with MULAN, further boosts the performance gap

to 10.1%. This further validates our LPG design choices and represents an additional contribution of this work, in addition to our main focus of lesion harvesting.

2) Alternative Missing Label Approaches:

We also evaluated other strategies for managing missing labels, namely overlap-based hard sampling (OBHS) [17] and overlap-based soft sampling (OBSS) [18], both of which are designed only for two-stage anchor-based detection networks, meaning they are incompatible with our one-stage MSCN. Thus, we use Faster R-CNN as baseline and compared OBHS and OBSS to training using our harvested prospective positive lesions, P_H^+ . OBHS only uses proposals with small overlap to a true positive as negative examples for the second stage classifier. As Table III demonstrates, the baseline Faster R-CNN performed with 34.2% AP, whereas using OBHS reduced the AP to 17.3%, demonstrating that simply ignoring the predominant background negatives causes large performance degradation. Thus, we also re-trained Faster R-CNN with a modified OBHS (M-OBHS), which preserves all background samples but raises weights of overlapping proposals to be twice as much as positive and standard background cases. This variant achieved 38.3% AP. As a different strategy, OBSS reduces the contributions of proposals which have small overlaps with the ground truth boxes but keeps all background cases. This strategy increased the AP to 36.3%. Finally, our method that trains Faster R-CNN with harvested prospective positive lesions achieved the best performance at 38.5% AP, with markedly higher recalls at lower tolerated FPs. This demonstrates that completing the label set with harvested

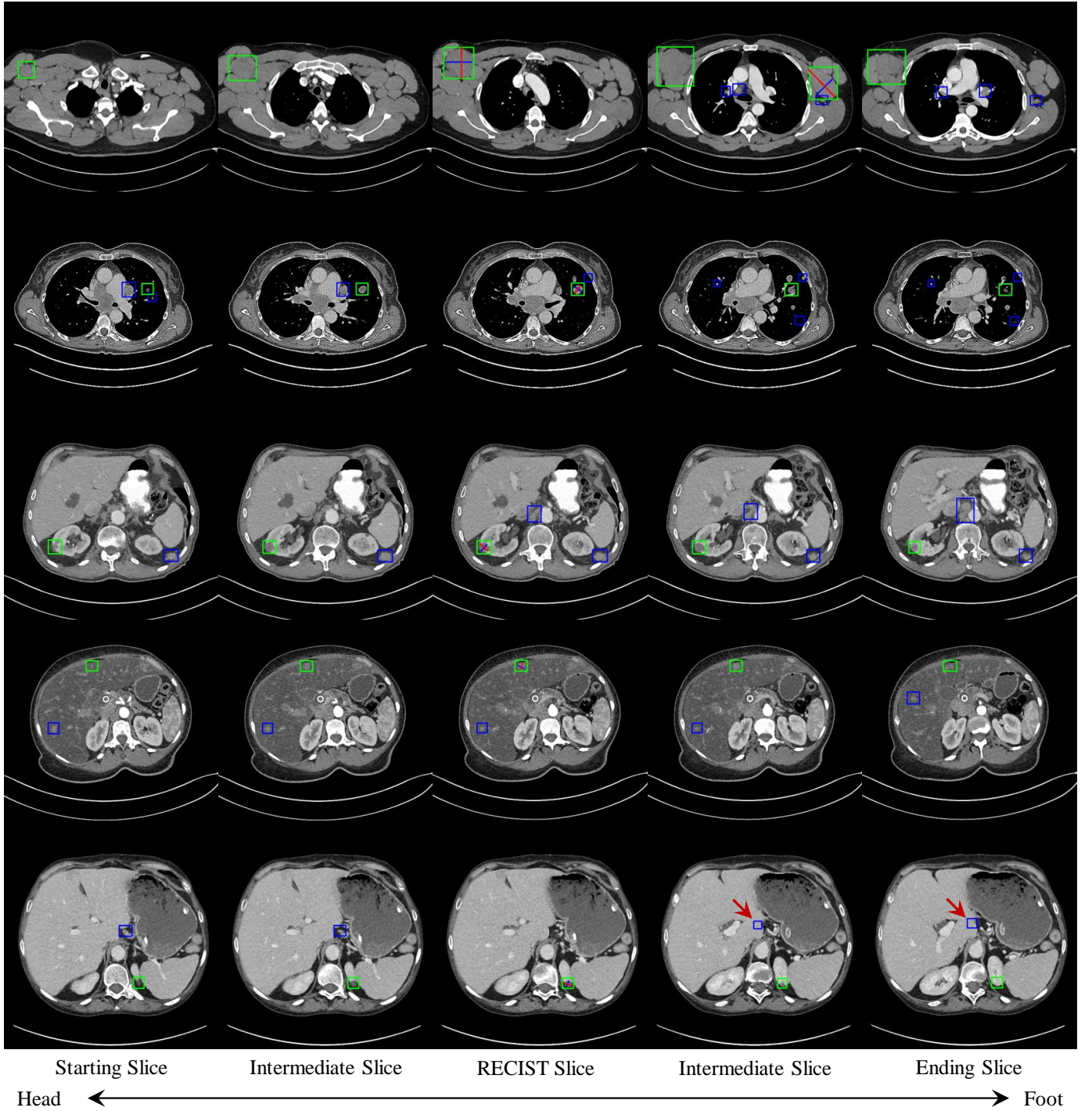


Fig. 6: Examples of 3D detection results and mined positive lesions from the harvesting set V_H . We use green and blue boxes to show RECIST-marked and mined lesions, respectively. Each 3D detection consists of multiple axial slices and we show 5 typical slices: the starting slice, the RECIST slice, the ending slice, and two intermediate slices. We show RECIST marks as crosses with red and blue lines. We also show one failure case at the bottom row indicated by red arrows.

lesions P_H^+ can provide greater boosts in performance than these alternative strategies. Yet, as we demonstrate, when using our harvested hard-negative proposals, along with one-stage detectors that can accommodate our HNSL, performance can be increased even further.

V. CONCLUSION

We present a powerful framework to harvest lesions from incompletely labeled datasets. Leveraging a very small subset of fully-labeled data, we chain together an LPG and LPC to iteratively discover and harvest unlabeled lesions. We test our system on the DeepLesion dataset and show that after only

annotating 5% of the volumes we can successfully harvest 9,805 additional lesions, which corresponds to 61.3% recall at 90% precision, which is a boost of 24.9% in recall over the original RECIST marks. Since, our proposed method is an open framework, it can accept any state-of-the-art LPG and LPC, allowing it to benefit from future improvements in these two domains.

Our work's impact has several facets. For one, in terms of DeepLesion specifically, the lesions we harvest and publicly release enhance the utility of an already invaluable dataset. As we demonstrated, training off-the-shelf detectors on our harvested lesions allows them to outperform the current best performance on the DeepLesion dataset by margins as high as 10% AP, which is a dramatic boost in performance. Furthermore, we expect our harvested lesions will prove useful to many applications beyond detection, *e.g.* radionomics studies. More broadly, our results indicate that the lesion harvesting framework is a powerful means to complete PACS-derived datasets, which we anticipate will be an increasingly important topic. Thus, this approach may help further expand the scale of data for the medical imaging analysis field.

Important contributions also include our proposed MSCN LPG, which outperforms the current state-of-the-art MULAN detector and helps push forward the lesion detection topic. In addition, the introduced P3D IoU metric acts as a much better evaluation metric for detection performance than current practices. As such, the adoption of the P3D metric as a standard for DeepLesion evaluation should better rank methods going forward. Future work should include investigating different LPG paradigms, *e.g.* full 3D approaches; measuring the impact of differing labor budgets on harvesting performance; and exploring active learning to more efficiently choose which volumes to label.

REFERENCES

- [1] P. Rajpurkar, J. Irvin, A. Bagul, and et al., "MURA dataset: Towards radiologist-level abnormality detection in musculoskeletal radiographs," *MIDL*, vol. abs/1712.06957, 2018.
- [2] X. Wang, L. Lu, H. Shin, L. Kim, I. Nogues, M. Bagheri, and R. M. Summers, "Unsupervised joint mining of deep features and image labels for large-scale radiology image categorization and scene recognition," in *IEEE WACV*, 2017, pp. 998–1007.
- [3] X. Wang, Y. Peng, L. Lu, Z. Lu, M. Bagheri, and R. M. Summers, "Chestx-ray8: Hospital-scale chest x-ray database and benchmarks on weakly-supervised classification and localization of common thorax diseases," in *IEEE Conference on Computer Vision and Pattern Recognition*, 2017, pp. 3462–3471.
- [4] K. Yan, X. Wang, L. Lu, and R. M. Summers, "Deeplesion: automated mining of large-scale lesion annotations and universal lesion detection with deep learning," *J. Med Imaging*, vol. 5, no. 3, 2018.
- [5] K. Yan, X. Wang, L. Lu, L. Zhang, A. Harrison, M. Bagheri, and R. M. Summers, "Deep lesion graphs in the wild: Relationship learning and organization of significant radiology image findings in a diverse large-scale lesion database," in *IEEE CVPR*, 2018.
- [6] M. D. Kohli, R. M. Summers, and J. R. Geis, "Medical image data and datasets in the era of machine learning: Whitepaper from the 2016 c-mimi meeting dataset session," in *Journal of Digital Imaging*, 2017.
- [7] H. Harvey and B. Glocker, "A standardised approach for preparing imaging data for machine learning tasks in radiology," in *Artificial Intelligence in Medical Imaging*. Springer, 2019, pp. 61–72.
- [8] J. Irvin, P. Rajpurkar, M. Ko, Y. Yu, S. Ciurea-Ilcus, C. Chute, H. Marklund, B. Haghighi, R. L. Ball, K. Shpanskaya, J. Seekins, D. A. Mong, S. S. Halabi, J. K. Sandberg, R. Jones, D. B. Larson, C. P. Langlotz, B. N. Patel, M. P. Lungren, and A. Y. Ng, "Chexpert: A large chest radiograph dataset with uncertainty labels and expert comparison," *CoRR*, vol. abs/1901.07031, 2019.
- [9] C. Erdi, S. Ecem, T. S. Ernst, M. Keelin, and v. G. Bram, "Handling label noise through model confidence and uncertainty: application to chest radiograph classification," 2019.
- [10] J. Deng, W. Dong, R. Socher, L.-J. Li, K. Li, and L. Fei-Fei, "ImageNet: A Large-Scale Hierarchical Image Database," in *IEEE CVPR*, 2009.
- [11] T.-Y. Lin, M. Maire, S. J. Belongie, L. D. Bourdev, R. B. Girshick, J. Hays, P. Perona, D. Ramanan, P. Dollr, and C. L. Zitnick, "Microsoft coco: Common objects in context," in *ECCV*, 2014.
- [12] E. Eisenhauer, P. Therasse, J. Bogaerts, and et al., "New response evaluation criteria in solid tumours: revised recist guideline (version 1.1)," *European journal of cancer*, vol. 45(2), pp. 228–247, 2009.
- [13] K. Yan, M. Bagheri, and R. M. Summers, "3d context enhanced region-based convolutional neural network for end-to-end lesion detection," in *MICCAI*, 2018, pp. 511–519.
- [14] X. Zhou, D. Wang, and P. Krähenbühl, "Objects as points," *CoRR*, vol. abs/1904.07850, 2019.
- [15] K. Yan, Y. Tang, Y. Peng, V. Sandfort, M. Bagheri, Z. Lu, and R. M. Summers, "MULAN: multitask universal lesion analysis network for joint lesion detection, tagging, and segmentation," *CoRR*, vol. abs/1908.04373, 2019.
- [16] K. He, G. Gkioxari, P. Dollár, and R. B. Girshick, "Mask R-CNN," in *IEEE International Conference on Computer Vision, ICCV 2017, Venice, Italy, October 22-29, 2017*, pp. 2980–2988.
- [17] S. Ren, K. He, R. Girshick, and J. Sun, "Faster R-CNN: Towards real-time object detection with region proposal networks," in *Advances in Neural Information Processing Systems (NIPS)*, 2015.
- [18] Z. Wu, N. Bodla, B. Singh, M. Najibi, R. Chellappa, and L. S. Davis, "Soft sampling for robust object detection," *CoRR*, vol. abs/1806.06986, 2018.
- [19] I. Radosavovic, P. Dollár, R. B. Girshick, G. Gkioxari, and K. He, "Data distillation: Towards omni-supervised learning," *IEEE CVPR*, vol. abs/1712.04440, 2018.
- [20] M. Gao, Z. Xu, L. Lu, A. Wu, I. Nogues, R. M. Summers, and D. J. Mollura, "Segmentation label propagation using deep convolutional neural networks and dense conditional random field," in *13th IEEE International Symposium on Biomedical Imaging, ISBI 2016, Prague, Czech Republic, April 13-16, 2016*, 2016, pp. 1265–1268.
- [21] J. Cai, Y. Tang, L. Lu, A. P. Harrison, K. Yan, J. Xiao, L. Yang, and R. M. Summers, "Accurate weakly-supervised deep lesion segmentation using large-scale clinical annotations: Slice-propagated 3d mask generation from 2d RECIST," in *Medical Image Computing and Computer Assisted Intervention - MICCAI, Part IV*, 2018, pp. 396–404.
- [22] C. Rother, V. Kolmogorov, and A. Blake, "'grabcut': interactive foreground extraction using iterated graph cuts," *ACM Trans. Graph.*, vol. 23, no. 3, pp. 309–314, 2004.
- [23] Q. Shao, L. Gong, K. Ma, H. Liu, and Y. Zheng, "Attentive CT lesion detection using deep pyramid inference with multi-scale booster," *CoRR*, vol. abs/1907.03958, 2019.
- [24] M. Zlocha, Q. Dou, and B. Glocker, "Improving retinanet for CT lesion detection with dense masks from weak RECIST labels," *CoRR*, vol. abs/1906.02283, 2019.
- [25] Q. Dou, H. Chen, L. Yu, J. Qin, and P. Heng, "Multilevel contextual 3-d cnns for false positive reduction in pulmonary nodule detection," *IEEE Trans. Biomed. Engineering*, vol. 64, no. 7, pp. 1558–1567, 2017.
- [26] J. Ding, A. Li, Z. Hu, and L. Wang, "Accurate pulmonary nodule detection in computed tomography images using deep convolutional neural networks," in *Medical Image Computing and Computer Assisted Intervention - MICCAI 2017 - 20th International Conference, Quebec City, QC, Canada, September 11-13, 2017, Proceedings, Part III*, 2017, pp. 559–567.
- [27] Y. Tang, K. Yan, Y. Tang, J. Liu, J. Xiao, and R. M. Summers, "Uldor: A universal lesion detector for ct scans with pseudo masks and hard negative example mining," in *16th IEEE International Symposium on Biomedical Imaging, ISBI 2019, Venice, Italy, April 8-11, 2019*, 2019, pp. 833–836.
- [28] K. Yan, X. Wang, L. Lu, and R. M. Summers, "Deeplesion: Automated deep mining, categorization and detection of significant radiology image findings using large-scale clinical lesion annotations," *CoRR*, vol. abs/1710.01766, 2017.
- [29] T. Lin, P. Goyal, R. B. Girshick, K. He, and P. Dollár, "Focal loss for dense object detection," in *IEEE International Conference on Computer Vision, ICCV 2017, Venice, Italy, October 22-29, 2017*, 2017, pp. 2999–3007.

- [30] G. Huang, Z. Liu, L. van der Maaten, and K. Q. Weinberger, "Densely connected convolutional networks," in *2017 IEEE Conference on Computer Vision and Pattern Recognition, CVPR 2017, Honolulu, HI, USA, July 21-26, 2017*, 2017, pp. 2261–2269.
- [31] F. Yang, H. Chen, J. Li, F. Li, L. Wang, and X. Yan, "Single shot multibox detector with kalman filter for online pedestrian detection in video," *IEEE Access*, vol. 7, pp. 15 478–15 488, 2019.
- [32] H. R. Roth, L. Lu, A. Seff, K. M. Cherry, J. Hoffman, S. Wang, J. Liu, E. Turkbey, and R. M. Summers, "A new 2.5d representation for lymph node detection using random sets of deep convolutional neural network observations," in *Medical Image Computing and Computer-Assisted Intervention - MICCAI 2014 - 17th International Conference, Boston, MA, USA, September 14-18, 2014, Proceedings, Part I*, 2014, pp. 520–527.
- [33] K. He, X. Zhang, S. Ren, and J. Sun, "Deep residual learning for image recognition," in *2016 IEEE Conference on Computer Vision and Pattern Recognition, CVPR 2016, Las Vegas, NV, USA, June 27-30, 2016*, 2016, pp. 770–778.
- [34] K. Hara, H. Kataoka, and Y. Satoh, "Can spatiotemporal 3d cnns retrace the history of 2d cnns and imagenet?" in *Proceedings of the IEEE Conference on Computer Vision and Pattern Recognition (CVPR)*, 2018, pp. 6546–6555.